Nanoscale

PAPER

View Article Online
View Journal | View Issue

Published on 21 November 2019. Downloaded by University of Washington on 7/29/2020 10:21:00 PM.

Check for updates

Cite this: Nanoscale, 2019, 11, 23188

High-throughput sequential excitation for nanoscale mapping of electrochemical strain in granular ceria†

Boyuan Huang, [a,b] Ehsan Nasr Esfahani, [a] Junxi Yu, [b,c] Brian S. Gerwe, [d] Stuart B. Adler [d] and Jiangyu Li *[a,b]

Dynamic strain based atomic force microscopy (AFM) modes often fail at the interfaces where the most interesting physics occurs because of their incapability of tracking contact resonance accurately under rough topography. To overcome this difficulty, we develop a high-throughput sequential excitation AFM that captures contact dynamics of probe–sample interactions with high fidelity and efficiency, acquiring the spectrum of data on each pixel over a range of frequencies that are excited in a sequential manner. Using electrochemically active granular ceria as an example, we map both linear and quadratic electrochemical strain accurately across grain boundaries with high spatial resolution where the conventional approach fails. The enhanced electrochemical responses point to the accumulation of small polarons in the space charge region at the grain boundaries, thought to be responsible for the enhanced electronic conductivity in nanocrystalline ceria. The spectrum of data can be processed very efficiently by physics-informed principal component analysis (PCA), speeding data processing by several orders of magnitude. This approach can be applied to a variety of AFM modes for studying a wide range of materials and structures on the nanoscale.

Received 28th August 2019,
Accepted 20th November 2019

DOI: 10.1039/c9nr07438d

rsc.li/nanoscale

Introduction

Atomic force microscopy (AFM) was invented in 1986,[1] and has since emerged as a powerful tool to probe a wide range of materials, structures, and systems with nanometer resolution.[2–6] Underlying the working principle of AFM is the dynamics of its cantilever, which is very sensitive to the sample–tip interactions, making it possible to probe a wide variety of functional properties.[7–13] Central to this operation is the resonance of the cantilever, tracking of which is essential to accurately capture the material characteristics of interest, or substantial crosstalk and artifacts will be resulted.[14] This is particularly important for an AFM operating in contact mode, such as piezoresponse force microscopy (PFM)[7,15–17] and electrochemical strain microscopy (ESM),[11,18–21] wherein contact resonance is greatly affected not only by material heterogeneity but also by surface topography. For samples with rough surfaces, for example, granular materials that are widely used in electrochemical conversions,[21–23] accurate contact resonance tracking is rather challenging, and the spatial resolution is often compromised as a result.

A number of techniques have been developed to address this issue. For example, dual amplitude resonance tracking (DART) excites the cantilever using two frequencies across the resonance, and utilizes the difference in their amplitudes as the error signal for tracking.[24,25] This works reasonably well for a smooth surface, but tracking often fails under a rough topography.[13,14,26] Band excitation (BE) has also been developed by synthesizing a signal summing all harmonic excitations within a frequency band,[27] so that resonance is covered within the band and thus tracking becomes unnecessary. Nevertheless, the excitation power of BE is distributed among the band of frequencies, resulting in much reduced strength and signal-to-noise ratios (S/N) at each individual frequency.[27] Alternatively, a series of excitation signals of varying frequencies can be applied to the cantilever in a sequential instead of a concurrent manner, one frequency at a time, so that the signal strength and S/N are not compromised.[26] Such sequential excitation (SE) turns out to be very effective at capturing

[a]Department of Mechanical Engineering, University of Washington, Seattle, WA 98195, USA. E-mail: jjli@uw.edu
[b]Shenzhen Key Laboratory of Nanobiomechanics, Shenzhen Institutes of Advanced Technology, Chinese Academy of Sciences, Shenzhen, Guangdong, 518055, China
[c]Key Laboratory of Low Dimensional Materials and Application Technology of Ministry of Education, and School of Materials Science and Engineering, Xiangtan University, Xiangtan, Hunan, 411105, China
[d]Department of Chemical Engineering, University of Washington, Seattle, WA 98195, USA

†Electronic supplementary information (ESI) available. See DOI: 10.1039/c9nr07438d

This journal is © The Royal Society of Chemistry 2019

Published on 21 November 2019. Downloaded by University of Washington on 7/29/2020 10:21:00 PM.

the cantilever dynamics,[26] though it requires multiple scans that are not only slow and inefficient but also tend to induce drifting, probe wearing and surface damage that complicates the analysis. For sensitive electrochemical materials that are not very stable, such as halide perovskites,[28,29] we may not even have time to complete all the necessary scans.

Here we develop a high-throughput SE AFM that is capable of accurately capturing the cantilever dynamics, and thus the underlying physical interactions, in just one instead of multiple scans. It has a scanning speed comparable to conventional DART, yet with much enhanced spatial resolution and quantitative accuracy, especially at the interface where steep steps locate. This approach can be applied to any AFM modes that rely on cantilever resonance for imaging, and we demonstrate this here using ESM to probe defect-induced Vegard strain near the grain boundaries in polycrystalline ceria. These defects (small polarons) are thought to accumulate near the grain boundaries, leading to enhanced electronic conductivity in nanoscrystalline ceria.[30,31] Using SE, we have mapped both the linear and quadratic electrochemical strains in ceria near the grain boundaries at much higher resolution and fidelity than that afforded by DART.

Results

Failure of resonance tracking

Atomic force microscopy (AFM) works by probing its cantilever dynamics as affected by sample–tip interactions, which can be accurately described using a damped harmonic oscillator model (DHO),[32]

$$A(\omega) = \frac{A_0\omega_0^2}{\sqrt{\left(\omega_0^2-\omega^2\right)^2+\left(\frac{\omega_0\omega}{Q}\right)^2}},$$
$$\phi(\omega) = \tan^{-1}\left[\frac{\omega_0\omega}{Q\left(\omega_0^2-\omega^2\right)}\right]+\phi_0, \quad (1)$$

where A_0, ϕ_0, Q, and ω_0 are the intrinsic amplitude, phase, quality factor and resonance frequency of the system, respectively, that are of interest to us, while $A(\omega)$ and $\phi(\omega)$ are the measured amplitude and phase at excitation frequency ω. In order to track the shifting resonance during a scan, which is essential to accurately capture the sample–tip interactions, DART measures two pairs of amplitudes and phases as $[A_1(\omega_1), \phi_1(\omega_1)]$ and $[A_2(\omega_2),\phi_2(\omega_2)]$ at two excitation frequencies ω_1 and ω_2, utilizing the difference between $A_1(\omega_1)$ and $A_2(\omega_2)$ as an error signal for feedback control. One set of $A_1(\omega_1)$ mappings carefully acquired during trace and retrace scanning using DART on granular ceria overlaid on its 3D topography are shown in Fig. 1a, which covers one grain and a number of grain boundaries, with more data presented in Fig. S1 of the ESI.† The scale of the color bar is set for the best image contrast, so the values on the color bar shown in Fig. 1a do not indicate the real range [1.3, 3.5]. While the trace and retrace mappings resemble each other well in most part of the scans, a closer examination reveals that they differ substantially at grain boundaries. This is made clearer by the comparison of the line scans shown in Fig. 1b, where it is evident that during tracing, the amplitude is reduced at the grain boundaries while during retracing, it is enhanced. As such, the trends are completely opposite between tracing and retracing at the grain boundaries, while away from the grain boundaries they agree well with each other. This difference highlights the failure of resonance tracking when there is significant topography variation often encountered in materials, even though the scan is carried out slowly with carefully adjusted parameters to ensure reliable tracking. For more casual scans, the problem will be more serious, as shown in Fig. 1c with more data in Fig. S2,† where there are noticeable wavelet scratch-like patterns in the mapping of frequency ω_1 that extends along the scanning direction of the probe, especially at the grain boundaries. Such an artifact clearly indicates the failure of resonance tracking, even within a grain where topography variation is insignificant, and such mappings are not reliable even for qualitative analysis.

High-throughput sequential excitation

One solution to overcome the difficulties of resonance tracking is to eliminate it altogether, for example by exciting the cantilever over a range of frequencies that cover the resonance. Band excitation (BE) implements this concept by applying all the frequencies concurrently,[27] while sequential excitation (SE) carries this out in a sequential manner.[26,33] The difference between these two approaches seems subtle, yet the implication is significant. The excitation power under SE is concentrated in each individual frequency, while under BE it is dis-

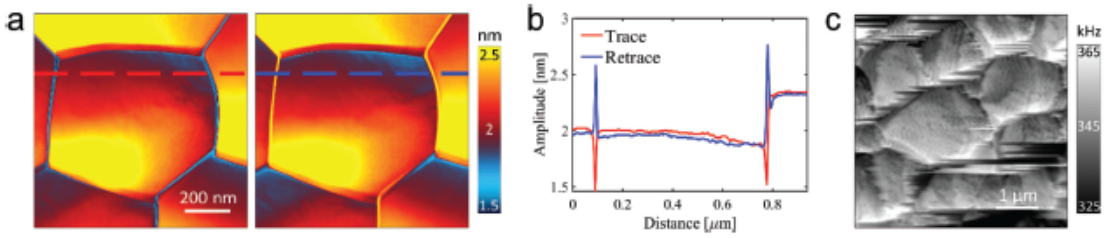

Fig. 1 The difficulty and failure of resonance tracking: (a) amplitude mappings from trace and retrace acquired under DART; (b) comparison of the corresponding line scans between trace and retrace; (c) artifacts in the mapping of excitation frequency.

Published on 21 November 2019. Downloaded by University of Washington on 7/29/2020 10:21:00 PM.

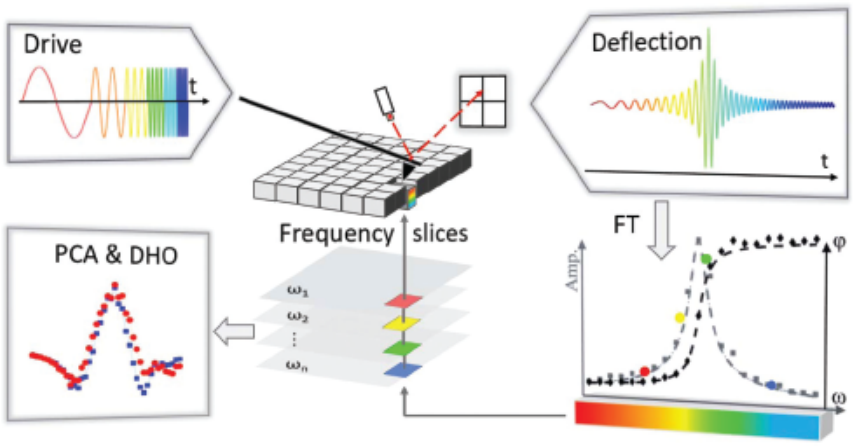

Fig. 2 Schematic of high-throughput SE-ESM.

tributed over the entire band, and thus SE has much stronger signal strength and S/N. Original SE requires multiple scans each with a distinct excitation frequency, which can be implemented on any standard AFM. Yet it is time consuming and prone to shifting during different scans, and it tends to induce probe wearing and sample damage. Here, we develop an advanced implementation for high-throughput SE that requires just one scan, as schematically shown in Fig. 2.

Central to our approach is a high-resolution waveform designated as Drive in Fig. 2 drawn in the time domain, where it is seen that the frequency increases over time. This drive signal consists of m joined sinusoidal waves with discrete frequencies, which can be produced by an Arbitrary Waveform Generator (AWG) for each pixel during scan, as detailed in Fig. S3.† The resulting deflection signal of the cantilever at each pixel is recorded in the time domain, and then Fourier transformed into the frequency domain using the corresponding drive as a reference. This is equivalent to a digital lock-in, from which m pairs of amplitudes and phases are obtained at each pixel over the frequency range of interest. As a demonstration, the actual excitation and response in one of our experiments are presented in Fig. 3. The drive consists of 15 sinusoidal waveforms with distinct frequencies ranging from 347 to 390 kHz connected in a sequential manner over a time span of 2.14 ms, as seen in Fig. 3a, with a zoomed in image of 3 such waveforms shown in Fig. 3b. Each waveform lasts for 50 cycles, leaving sufficient time to acquire response data accurately, corresponding to a line scan rate of 0.8 Hz that is comparable to a typical DART – it takes just 5 min to complete a 256 × 256 pixel scan. The response is recorded in the time domain, as shown in Fig. 3c and d, which contains a large volume of data and is quite noisy. Yet after being Fourier transformed into the frequency domain, a clear resonant peak emerges in amplitude, due to which the phase jumps by 180°, as shown in Fig. 3e and f along with the drive signal. Such dynamics is expected from DHO governed by eqn (1), and this illustrates how high-throughput SE works on signal generation as well as data acquisition and processing.

Linear and quadratic electrochemical strains

We now apply high throughput SE to probe linear and quadratic electrochemical strains of granular ceria *via* first and second harmonic ESM measurements,[34,35] for which high fidelity mappings at the grain boundaries are essential to examine the proposed accumulation of space charges in its interfacial regions. Since a sequence of $A(\omega_i)$ and $\phi(\omega_i)$ are acquired under SE at each pixel, which can be fitted by eqn (1) of DHO as shown in Fig. S4,† we can obtain parameters intrinsic to the probed system, including the intrinsic amplitude, phase, quality factor, and resonant frequency. Note that both amplitude and phase equations can be used, yielding consistent mappings as shown in Fig. S4.†

Linear electrochemical strain obtained as such is shown in Fig. 4a, acquired *via* first harmonic measurements at each of the excitation frequencies, while quadratic strain is shown in Fig. 4b, acquired *via* second harmonic measurements at frequencies that double each excitation frequency. For both mappings, it is evident that the responses are substantially enhanced at the grain boundaries, which can be seen more clearly from point-wise comparison of the first and second harmonic responses at the grain boundaries and within a grain, as shown in Fig. 4i. Furthermore, histogram distributions of the first and second harmonic responses in Fig. 4c reveal that the electrochemical strain is predominantly linear, arising from Vegard strain due to fluctuations in the small polaron concentration under the AC excitation, while the quadratic strain due to an electrochemical dipole and thus electrostriction is also present.[35] Further insight can be gained from the mappings of quality factors associated with the first (Fig. 4d) and second (Fig. 4e) harmonic measurements, where it is observed that the second harmonic electrostriction has a higher quality factor (Fig. 4f), and thus smaller dissipation, as

 This journal is © The Royal Society of Chemistry 2019

Published on 21 November 2019. Downloaded by University of Washington on 7/29/2020 10:21:00 PM.

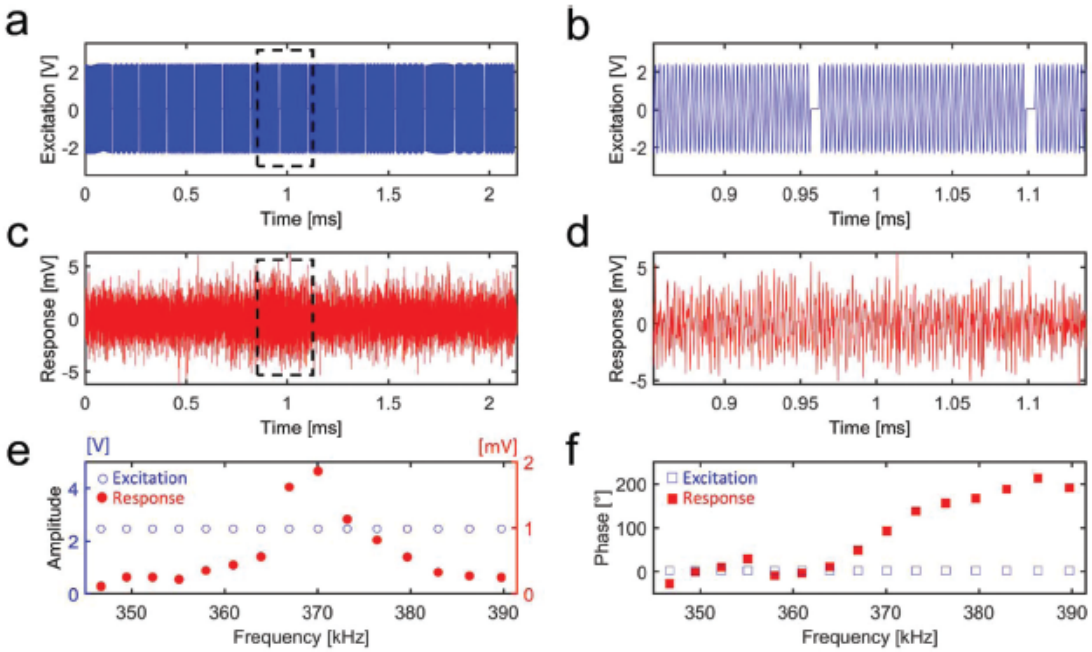

Fig. 3 Excitation and response of SE in time- and frequency-domains; (a, b) drive in the time domain; (c, d) response in the time domain; (e, f) drive and response in the frequency domain.

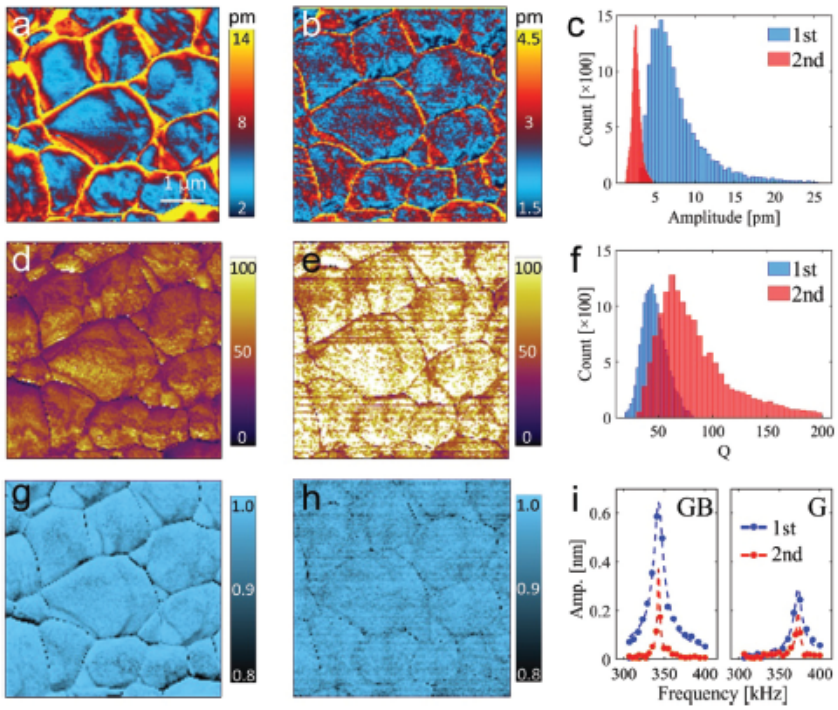

Fig. 4 Linear and quadratic strains in granular ceria; amplitude mappings of the first (a) and second (b) harmonic responses, and their histogram distribution (c); quality factor mappings of the first (d) and second harmonic measurements (e), and their histogram distribution (f); mappings of the R^2 of the first (g) and second (h) harmonic responses indicating DHO fitting fidelity; and (i) point-wise first and second harmonic response at the grain boundaries with a grain.

Published on 21 November 2019. Downloaded by University of Washington on 7/29/2020 10:21:00 PM.

Vegard strain from small polarons is an energy-dissipative process. These observations are consistent with the proposed accumulation of space charges at the grain boundaries, resulting in enhanced response at the grain boundaries in both first and second harmonics.

We also examine the mappings of resonant frequencies from the first and second harmonic measurements presented in Fig. S5,† which match well with each other, demonstrating the high fidelity of the measurement. More importantly, we can examine the accuracy of the DHO fitting at each pixel in terms of the R^2 coefficient,[36] a statistical measure on how close the data points are to the fitted regression line. Mappings of the R^2 coefficients are presented in Fig. 4g and h for the first and second harmonic measurements, ranging from 0.8 to 1.0 with respective mean values of 0.97 and 0.96, demonstrating high fidelity of the fitting. Even at the grain boundaries, the fitting coefficients are mostly over 0.91. This is another advantage of SE, wherein the sequence of data enables us to accurately assess the reliability of the DHO fitting for quantitative analysis. Under conventional DART, on the other hand, only two data points are available to solve the highly nonlinear DHO equations, which is not expected to be very accurate. Indeed, we compare the mappings of the intrinsic amplitude, quality factor, and resonant frequencies acquired from DART and SE in Fig. 5, and it is evident that DART not only fails near the grain boundaries, as marked by all the white dots wherein there is no solution found for DHO, but it is also quantitatively different from SE, made evident by the comparison of histogram distributions in the amplitude – it underestimates the amplitude response substantially. Nevertheless, it is also quite remarkable to note that DART appears to be able to track the resonant frequency pretty well for the most part of grains, and majority of the issues occur at the grain boundaries.

Data-accelerated physical analysis

While DHO is able to fit SE data accurately, it is a relatively slow process not amenable to real time control and adjustment, which is necessary for machine learning and artificial intelligence AFM that could be enabled by the big data generated under SE.[37] On the other hand, a large volume of spectral information collected by SE is well suited for data analytics such as principal component analysis (PCA), which is highly efficient, though such pure statistical analytics often lacks clear physical insight. By carefully comparing the underlying mathematics of both approaches, we are able to draw a close connection between PCA modes and DHO expansion,[26] rendering clear physical significance to otherwise purely statistical PCA modes. To this end, we first recast the 3D dataset of $\mathbf{A}(\omega, x, y)$ into a 2D matrix of $\mathbf{A}(\omega, n)$, where the 2D spatial grid collapsed into 1D. Here each row of $\mathbf{A}$ contains spatial data from

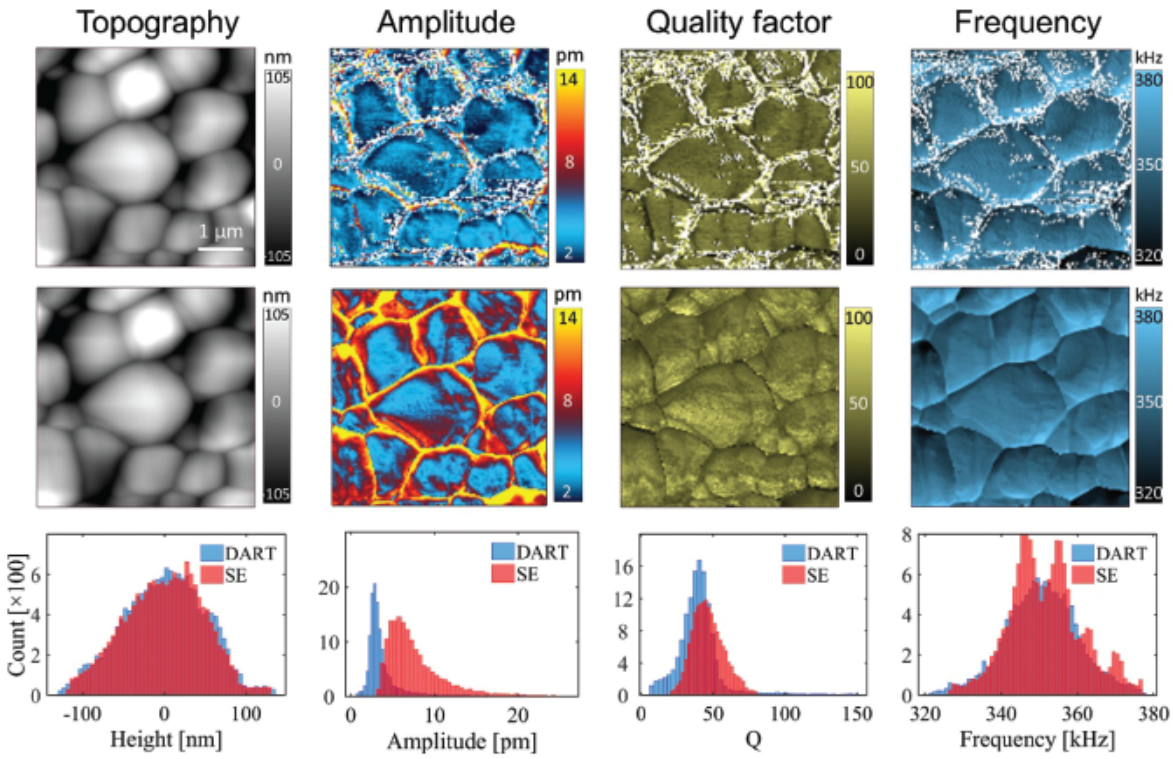

Fig. 5 Comparison of the ESM mappings of ceria acquired by DART (first row) and SE (second row), along with their histogram distribution (third row).

 This journal is © The Royal Society of Chemistry 2019

Published on 21 November 2019. Downloaded by University of Washington on 7/29/2020 10:21:00 PM.

a mapping scanned at a particular frequency, while each column represents the spectral responses of a particular grid point acquired under various excitations. Principal component analysis (PCA) of $\mathbf{A}(\omega,n)$ can then be carried out through singular value decomposition (SVD),[38]

$$\mathbf{A} = \sum_{i=1}^{r} \sigma_i u_i w_i^T$$

where $\{u_i\}$ and $\{w_i\}$ are the left and right singular vectors of $\mathbf{A}$, corresponding to the principal spectral and spatial modes sorted by their singular values $\{\sigma_i\}$. In other words, any row/column of $\mathbf{A}$ can be represented with a combination of $\{u_i\}$ or $\{w_i\}$, separately.

In a parallel manner, we can also construct a new set of orthonormal modes from the Taylor expansion series of DHO eqn (1) *via* the Gram–Schmidt process,[38] with $\boldsymbol{\beta}_1 = \mathbf{A}_0\mathbf{Q}\boldsymbol{\omega}_0$, and $\boldsymbol{\beta}_2$ and $\boldsymbol{\beta}_3$ derived from $\boldsymbol{\alpha}_2 = \mathbf{A}_0\mathbf{Q}\boldsymbol{\omega}_0 \cdot (\boldsymbol{\omega}_0 - \bar{\boldsymbol{\omega}}_0)$ and $\boldsymbol{\alpha}_3 = \mathbf{A}_0\mathbf{Q}\boldsymbol{\omega}_0 \cdot (\boldsymbol{\omega}_0 - \bar{\boldsymbol{\omega}}_0)^2$, where the operator $\cdot$ denotes the Hadamard product of two vectors, $\mathbf{A}_0\mathbf{Q}\boldsymbol{\omega}_0 = \mathbf{A}_0 \cdot \mathbf{Q} \cdot \boldsymbol{\omega}_0$, while the overhead bar denotes spatial averaging. It turns out that there is one-to-one correspondence between the PCA modes and DHO expansion basis,[26] which is confirmed by the good agreement, as shown in Fig. 6. The structural similarity (SSIM) (99.1%, 95.8%, and 94.3%) and Pearson correlation coefficients (PCC) (80.4%, 90.7%, and 83.9%) between the PCA spatial modes and DHO basis in Fig. 6b and c are pretty high, validating our analysis numerically. Note that PCA is much more efficient than DHO fitting, speeding up the data processing by 4 orders of magnitude, while we show that it provides essentially the same physical insight as DHO.

Discussion

With ever-increasing hardware capabilities and computational powers, we are on the brink of a big data revolution for physical science[39–41] and AFM provides an ideal playground for the data-driven nanoscience that promises unprecedented new insight.[26,41–43] A good example is the recently developed G-mode AFM that relies on brute force big data analytics without pre-committing to a particular physical process,[41,44]

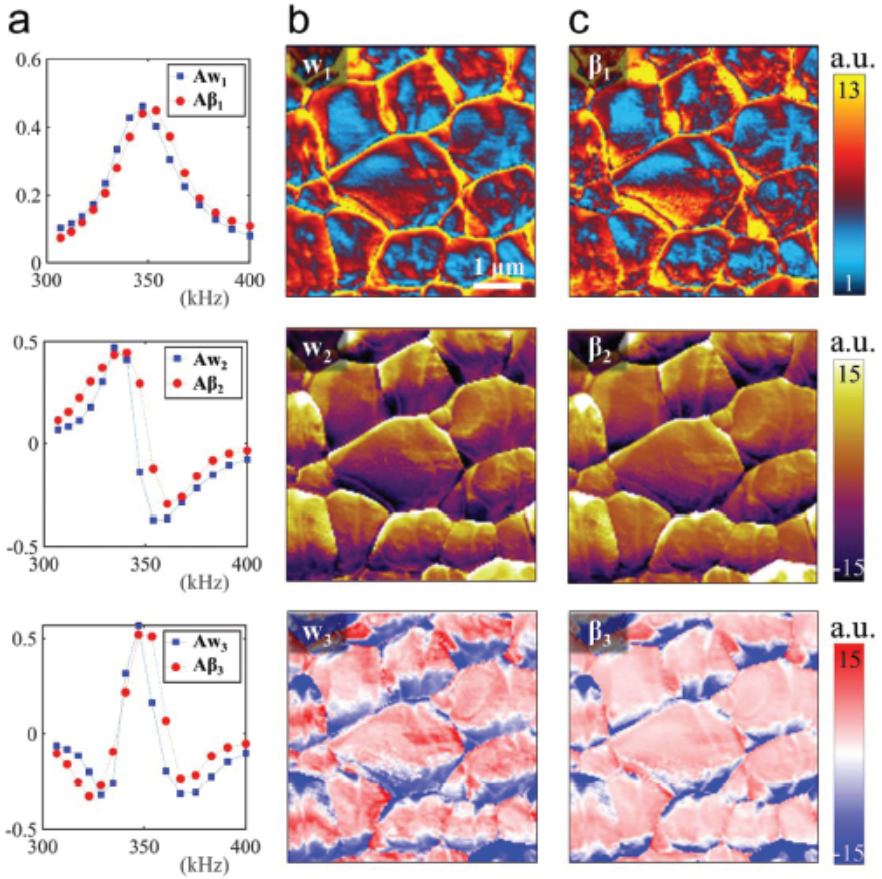

Fig. 6 Comparison of PCA modes and DHO expansion for the first harmonic ESM data of granular ceria; (a) first three PCA spectral modes in comparison with the corresponding DHO spectral basis; (b) first three PCA spatial modes; (c) corresponding DHO spatial basis.

Published on 21 November 2019. Downloaded by University of Washington on 7/29/2020 10:21:00 PM.

which is capable of uncovering "*unknown*" mechanisms underlying the physical systems. Here we adopt a more targeted approach, taking advantage of both physical understanding and data power. In particular, we design our excitation signals and data analysis specifically to capture cantilever resonance accurately, without acquiring too many redundant data, and ensuring that the data are clean and relevant to our physical system under the probe. As a result, our experimentation and analysis are highly efficient and accurate, which can be further accelerated by DHO-informed PCA analysis. Depending on particular systems under investigation, other forms of excitation signals can be designed and analyzed in a similar manner, for example by varying the excitation amplitude for ferroelectric switching, it is possible to implement a particular form of excitation on demand. In a sense, our approach is well aligned with the movement from big data to deep data, *i.e.*, from data mining, correlation analysis, and unsupervised classification to causative data analytics that fuses physical understanding into big data.[2,40,45–48] For this purpose, innovative experimental and/or computational methodologies to acquire high quality (less noisy), efficient (less redundant), and physically relevant scientific data are essential, and this work is an attempt along this direction.

The power of our approach is best illustrated at the grain boundaries of ceria, wherein enhanced electrochemical strain is evident, attributed to the accumulation of space charges. Since SE does not depend on resonance tracking, it outperforms the conventional approach as expected when it comes to large spatial variation. Moreover, SE is able to justify the fitting results and the validity of raw data by taking advantages of multiple datapoints and statistics, while DART lacks this ability and is more vulnerable to various measurement errors with only two datapoints. As shown in Fig. 5, even though maps probed by DART on grains look relatively smooth, it may still underestimate response without awareness. Furthermore, we also conduct SE-ESM on a solid electrolyte $Li_{1.3}Al_{0.3}Ti_{1.7}(PO_4)_3$ at a high temperature (115 °C), which is usually challenging for conventional resonance tracking due to continuous deformation of the sample originating from environmental temperature variation. But the R^2 map of the SE approach in Fig. S6e† is overall greater than 0.9, implying it is still very trustworthy in a temperature-controlled environment, given that the fitting is based on multiple datapoints. Therefore, we believe that our high throughput SE will provide a powerful tool to resolve the spatial variation of such cases with nanometer resolution.

Conclusions

In conclusion, we have developed a high-throughput AFM that captures the electrochemical strain of ceria in just one scan, having scanning speed comparable to conventional DART, yet with much enhanced spatial resolution and high quantitative fidelity. This enables us to image the accumulation of space charges across the grain boundaries of ceria with nanometer resolution, and DHO-informed PCA has also been developed, speeding up the data analysis by several orders of magnitude. These ideas can be applied to a variety of AFM modes for studying a wide range of materials and structures on the nanoscale, especially at the interfaces, and it embodies the spirit of deep data wherein targeted data acquisition and physics-informed data analytics prove to be powerful.

Methods

DART-ESM

This measurement is performed on a Cypher AFM with an AC amplitude of 4 V applied to a Nanosensor PPP-EFM conductive probe. The scan rate is 1.0 Hz and the dynamics of the cantilever motion is characterized using built-in lock-in amplifiers, which physically reduces full time-domain information to limited frequency-domain data in terms of raw amplitudes and phases. The mappings of corrected amplitude, phase, resonant frequency, and quality factor were then calculated *via* the DHO model.

SE-ESM

Both first and second harmonic resonance SE-ESM scannings were implemented using a UHF-AWG in combination with a Cypher AFM. Before scanning, the UHF-AWG has synthesized the desired waveform associated digital markers. Once the digital trigger from the AFM is received, the AWG begins to convert the waveform into analog signals with a 3.5 MHz ADC rate, which will then be fed into the AFM to excite the probe. At the same time, a data acquisition (DAQ) system in UHF is also triggered and it started to record the full motion of the probe in the time domain *via* a deflection channel of the AFM, sampling at 3.5 MHz. The synchronization is well tuned beforehand by adjusting the input waveform so that the excitation can work in parallel with the AFM XY scanners with delays less than 0.7 ms for each line, which is about a quarter of the scanning time for one pixel. The turn-around time between trace/retrace passes is enough for the DAQ to transfer the data to a computer for FT on-the-fly. The same sample and probe were used for the DART-ESM measurement.

The design of the SE waveform

The unit waveform used for one pixel usually consists of 15 different segments, each of which contains multiple periods of sinusoidal waves with a specific frequency belonging to [300 kHz, 400 kHz]. The amplitude of all sinusoidal waves is the same as DART-ESM used. Segments are sorted by the frequencies and joined with 20 sampling points of zero amplitude, forming a unit waveform. Finally, the unit waveform is first joined with 100 sampling points of zero amplitude, which helps the relaxation of the probe and the post-processing of data, and then repeated multiple times for one trace of scanning. Parameters may be slightly changed in the real experiment to meet the requirement of synchronization mentioned above. For the first harmonic measurement, the input wave-

 This journal is © The Royal Society of Chemistry 2019

Published on 21 November 2019. Downloaded by University of Washington on 7/29/2020 10:21:00 PM.

form is also used as the reference wave of FT. For the second harmonic measurement, the input waveform is repeated once and then half sampled to generate the reference wave of FT, considering that the sample response was measured at the double frequency of the excitation.

Principal components analysis

PCA is a statistical procedure that converts a set of observations of possibly correlated variables into a set of linearly uncorrelated variables called principal components. In this work, PCA is computed *via* a SVD function in MATLAB, that is

$$\mathbf{A} = \mathbf{U}\mathbf{\Sigma}\mathbf{W}^{\mathrm{T}} = \sum_{i=1}^{r} \sigma_i u_i w_i^T$$

where r is the rank of **A**. Thus, spectral and spatial modes of dataset **A** correspond to the left and right singular vectors ($\{u_i\}$ and $\{w_i\}$) of **A**, which are ranked in the order of their importance (or say singular values $\{\sigma_i\}$). According to low rank approximation, **A** can be perfectly reconstructed using first p modes if the last $r - p + 1$ singular values are below the level of noise,

$$\mathbf{A} = \sum_{i=1}^{r} \sigma_i u_i w_i^T \approx \sum_{i=1}^{p} \sigma_i u_i w_i^T.$$

In this sense, PCA is an efficient algorithm for dimension reduction and data compression.

Structural similarity

SSIM is a perceptual metric that quantifies the similarity between two images. It is the average of the local SSIM value map:

$$\mathrm{SSIM}(x,y) = \frac{(2\mu_a\mu_b + c_1)(2\sigma_{ab} + c_2)}{(\mu_a{}^2 + \mu_b{}^2 + c_1)(\sigma_a{}^2 + \sigma_b{}^2 + c_2)},$$

where μ_a, μ_b, σ_a, σ_b, and σ_{ab} are the average, variance, and covariance of 4×4 windows a and b that are centered in the pixel (x, y) of two images. c_1 and c_2 are the two constants to stabilize the division with a weak denominator.

Pearson correlation coefficient

PCC can take a range of values from +1 to −1. A value of 0 implies that there is no linear correlation between two vectors X and Y that are reshaped from two images respectively, while +1 means total positive linear correlation and −1 means total negative linear correlation.

$$P_{X,Y} = \frac{\sigma_{XY}}{\varsigma_X \varsigma_Y}$$

where σ_{XY} is the covariance, and ς_X and ς_Y, are the standard deviation of X and Y, respectively.

Data availability

The data that support the findings of this study are available from the corresponding author upon request.

Author contributions

J. L. conceived and supervised the project. B. S. G. grew the ceria sample under the guidance of S. B. A. B. H. carried out AFM studies with the assistance of E. N. E. and J. Y. J. L. wrote the manuscript and all authors participated in the revision and discussion.

Conflicts of interest

The authors declare no competing financial or non-financial interest.

Acknowledgements

We acknowledge the support from the US NSF through the Materials Research Science and Engineering Center (DMR-1719797) SuperSeed Award and Chemical Measurement & Imaging Program (CHE-1708376). The instrumentation at SIAT was carried out with the support from the NSFC of China (11627801) and the Key Area R&D Program of Guangdong Province (2018B010109009).

References

1 G. Binnig, C. F. Quate and C. Gerber, *Phys. Rev. Lett.*, 1986, **56**, 930.
2 S. V. Kalinin, E. Strelcov, A. Belianinov, S. Somnath, R. K. Vasudevan, E. J. Lingerfelt, R. K. Archibald, C. Chen, R. Proksch, N. Laanait and S. Jesse, *ACS Nano*, 2016, **10**, 9068–9086.
3 S. V. Kalinin and A. Gruverman, *Scanning probe microscopy: electrical and electromechanical phenomena at the nanoscale*, Springer Science & Business Media, 2007, vol. 1.
4 T. Li and K. Zeng, *Adv. Mater.*, 2018, **30**, 1803064.
5 B. Huang, G. Kong, E. N. Esfahani, S. Chen, Q. Li, J. Yu, N. Xu, Y. Zhang, S. Xie, H. Wen, P. Gao, J. Zhao and J. Li, *npj Quantum Mater.*, 2018, **3**, 30.
6 G. Zhong, F. An, Y. Bitla, J. Wang, X. Zhong, J. Yu, W. Gao, Y. Zhang, C. Tan and Y. Ou, *ACS Nano*, 2018, **12**, 9558–9567.
7 A. Gruverman and S. V. Kalinin, *J. Mater. Sci.*, 2006, **41**, 107–116.
8 A. Majumdar, *Annu. Rev. Mater. Sci.*, 1999, **29**, 505–585.
9 T. W. Kelley, E. Granstrom and C. D. Frisbie, *Adv. Mater.*, 1999, **11**, 261–264.
10 J. Li, J.-F. Li, Q. Yu, Q. N. Chen and S. Xie, *J. Mater.*, 2015, **1**, 3–21.
11 A. N. Morozovska, E. A. Eliseev, N. Balke and S. V. Kalinin, *J. Appl. Phys.*, 2010, **108**, 53712.
12 S. Li, Y. Zhou, Y. Zi, G. Zhang and Z. L. Wang, *ACS Nano*, 2016, **10**, 2528–2535.
13 E. N. Esfahani, T. Li, B. Huang, X. Xu and J. Li, *Nano Energy*, 2018, **52**, 117–122.

Published on 21 November 2019. Downloaded by University of Washington on 7/29/2020 10:21:00 PM.

14 S. Bradler, A. Schirmeisen and B. Roling, *J. Appl. Phys.*, 2018, **123**, 035106.
15 D. A. Bonnell, S. V. Kalinin, A. L. Kholkin and A. Gruverman, *MRS Bull.*, 2009, **34**, 648–657.
16 R. K. Vasudevan, N. Balke, P. Maksymovych, S. Jesse and S. V. Kalinin, *Appl. Phys. Rev.*, 2017, **4**, 021302.
17 Y. Liu, H.-L. Cai, M. Zelisko, Y. Wang, J. Sun, F. Yan, F. Ma, P. Wang, Q. N. Chen and H. Zheng, *Proc. Natl. Acad. Sci. U. S. A.*, 2014, **111**, E2780–E2786.
18 J. Zhu, L. Lu and K. Zeng, *ACS Nano*, 2013, **7**, 1666–1675.
19 N. Balke, S. Jesse, A. N. Morozovska, E. Eliseev, D. W. Chung, Y. Kim, L. Adamczyk, R. E. García, N. Dudney and S. V. Kalinin, *Nat. Nanotechnol.*, 2010, **5**, 749.
20 R. Giridharagopal, L. Q. Flagg, J. S. Harrison, M. E. Ziffer, J. Onorato, C. K. Luscombe and D. S. Ginger, *Nat. Mater.*, 2017, **16**, 1–6.
21 S. Duan, H. Jin, J. Yu, E. N. Esfahani, B. Yang, J. Liu, Y. Ren, Y. Chen, L. Lu and X. Tian, *Nano Energy*, 2018, **51**, 19–25.
22 D. O. Alikin, K. N. Romanyuk, B. N. Slautin, D. Rosato, V. Y. Shur and A. L. Kholkin, *Nanoscale*, 2018, **10**, 2503–2511.
23 Q. N. Chen, Y. Liu, Y. Liu, S. Xie, G. Cao and J. Li, *Appl. Phys. Lett.*, 2012, **101**, 63901.
24 B. J. Rodriguez, C. Callahan, S. V. Kalinin and R. Proksch, *Nanotechnology*, 2007, **18**, 475504.
25 A. Gannepalli, D. G. Yablon, A. H. Tsou and R. Proksch, *Nanotechnology*, 2011, **22**, 355705.
26 B. Huang, E. N. Esfahani and J. Li, *Natl. Sci. Rev.*, 2018, **6**, 55–63.
27 S. Jesse, S. V. Kalinin, R. Proksch, A. P. Baddorf and B. J. Rodriguez, *Nanotechnology*, 2007, **18**, 435503.
28 S. Chen, X. Zhang, J. Zhao, Y. Zhang, G. Kong, Q. Li, N. Li, Y. Yu, N. Xu and J. Zhang, *Nat. Commun.*, 2018, **9**, 4807.
29 R. Wang, M. Mujahid, Y. Duan, Z.-K. Wang, J. Xue and Y. Yang, *Adv. Funct. Mater.*, 2019, 1808843.
30 Q. N. Chen, S. B. Adler and J. Li, *Appl. Phys. Lett.*, 2014, **105**, 1–5.
31 S. Kim and J. Maier, *J. Electrochem. Soc.*, 2002, **149**, J73–J83.
32 A. P. French, *Vibrations and waves*, CRC press, 1971.
33 P. Jiang, B. Huang, L. Wei, F. Yan, X. Huang, Y. Li, S. Xie, K. Pan, Y. Liu and J. Li, *Nanotechnology*, 2019, **30**, 205703.
34 Q. N. Chen, Y. Ou, F. Ma and J. Li, *Appl. Phys. Lett.*, 2014, **242907**, 1–5.
35 J. Yu, E. N. Esfahani, Q. Zhu, D. Shan, T. Jia, S. Xie and J. Li, *J. Appl. Phys.*, 2018, **123**, 155104.
36 S. A. Glantz and B. K. Slinker, *Primer of Applied Regression and Analysis of Variance*, 1990.
37 B. Huang, Z. Li and J. Li, *Nanoscale*, 2018, **10**, 21320–21326.
38 W. H. Greub, *Linear algebra*, Springer Science & Business Media, 2012, vol. 23.
39 J. Hill, G. Mulholland, K. Persson, R. Seshadri, C. Wolverton and B. Meredig, *MRS Bull.*, 2016, **41**, 399–409.
40 J. Byers, *Nat. Phys.*, 2017, **13**, 718.
41 A. Belianinov, S. V. Kalinin and S. Jesse, *Nat. Commun.*, 2015, **6**, 6550.
42 H. Trivedi, V. V. Shvartsman, M. S. A. Medeiros, R. C. Pullar and D. C. Lupascu, *npj Comput. Mater.*, 2018, **4**, 1–7.
43 R. Giridharagopal, J. T. Precht, S. Jariwala, L. Collins, S. Jesse, S. V. Kalinin and D. S. Ginger, *ACS Nano*, 2019, **13**, 2812–2821.
44 L. Collins, M. Ahmadi, T. Wu, B. Hu, S. V. Kalinin and S. Jesse, *ACS Nano*, 2017, **11**, 8717–8729.
45 S. Munevar, *Nat. Biotechnol.*, 2017, **35**, 684.
46 R. Yuan, Z. Liu, P. V. Balachandran, D. Xue, Y. Zhou, X. Ding, J. Sun, D. Xue and T. Lookman, *Adv. Mater.*, 2018, **30**, 1702884.
47 D. S. Kermany, M. Goldbaum, W. Cai, C. C. S. Valentim, H. Liang, S. L. Baxter, A. McKeown, G. Yang, X. Wu, F. Yan, J. Dong, M. K. Prasadha, J. Pei, M. Ting, J. Zhu, C. Li, S. Hewett, J. Dong, I. Ziyar, A. Shi, R. Zhang, L. Zheng, R. Hou, W. Shi, X. Fu, Y. Duan, V. A. N. Huu, C. Wen, E. D. Zhang, C. L. Zhang, O. Li, X. Wang, M. A. Singer, X. Sun, J. Xu, A. Tafreshi, M. A. Lewis, H. Xia and K. Zhang, *Cell*, 2018, **172**, 1122–1131.
48 Y. Liu, T. Zhao, W. Ju and S. Shi, *J. Mater.*, 2017, **3**, 159–177.

This journal is © The Royal Society of Chemistry 2019